

# Thermal Stability of Quasi-1D NbS<sub>3</sub> Nanoribbons and Their Transformation to 2D NbS<sub>2</sub>: Insights from *In Situ* Electron Microscopy and Spectroscopy

Eric V. Formo<sup>1\*</sup>, Jordan Hatchel<sup>2</sup>, Yassamin Ghafouri<sup>3</sup>, Matthew A. Bloodgood<sup>3</sup>, Tina T. Salguero<sup>3\*</sup>

- 1) Georgia Electron Microscopy, University of Georgia, Athens, GA USA
- 2) Center for Nanophase Materials, Oak Ridge National Laboratory, Oak Ridge, TN USA
- 3) Department of Chemistry, University of Georgia, Athens, GA USA

\* Authors to whom correspondence should be addressed

eformo@uga.edu

salguero@uga.edu

*Notice: This manuscript has been authored by UT-Battelle, LLC, under Contract No. DE-AC0500OR22725 with the U.S. Department of Energy. The United States Government retains and the publisher, by accepting the article for publication, acknowledges that the United States Government retains a non-exclusive, paid-up, irrevocable, world-wide license to publish or reproduce the published form of this manuscript, or allow others to do so, for the United States Government purposes. The Department of Energy will provide public access to these results of federally sponsored research in accordance with the DOE Public Access Plan (<http://energy.gov/downloads/doe-public-access-plan>).*

## Abstract

*In situ* electron microscopy imaging and spectroscopy enabled us to study the evolution of quasi-1D NbS<sub>3</sub>-IV nanoribbons with respect to morphology and chemical structure at temperatures between RT and 1000 °C. Scanning transmission electron microscopy (STEM) experiments included imaging in the secondary electron, (transmitted) bright field, and high angle dark field modes while operating in the low kV regime. The results showed that NbS<sub>3</sub>-IV samples transform dramatically from smooth nanoribbons into highly-textured configurations featuring polyhedral divots and steps. Similar *in situ* heating experiments conducted with aberration-corrected STEM revealed that bilayers of NbS<sub>3</sub>-IV chains convert topotactically into aligned 2H-NbS<sub>2</sub> sheets upon loss of sulfur. Atomic resolution imaging, Fast Fourier Transform (FFT) analysis, and Electron Energy Loss Spectroscopy (EELS) confirmed these chemical changes, from which we propose an atomistic mechanism for the NbS<sub>3</sub>-IV → 2H-NbS<sub>2</sub> conversion.

## Introduction

Recent work has revealed that quasi-1D transition metal trichalcogenide nanomaterials can exhibit outstanding properties, such as charge density waves, the ability to support high current densities prior to breakdown, low levels of electronic noise, and anisotropic optical characteristics (1-5), which make them excellent candidates for next-generation device applications. Niobium trisulfide,  $\text{NbS}_3$ , is an especially interesting system because its polymorphism stands out among transition metal trichalcogenides, with up to five  $\text{NbS}_3$  crystal structures verified to date (6-9). All contain 1D chains of stacked, niobium hexasulfide trigonal prisms assembled into bilayer sheets through interchain Nb---S and S---S interactions. The polymorphs differ in (i) the degree of metal bonding along the chains, *i.e.*, the presence or absence of niobium pairing (structural Peierls distortion), and (ii) the repeating pattern and alignment of the bilayer sheets interacting through van der Waals forces.  $\text{NbS}_3$ -IV, the subject of the present study, exhibits chains oriented along the *a*-axis that contain niobium pairing and are arranged into repeating sets of bilayers (Figure 1) (7).

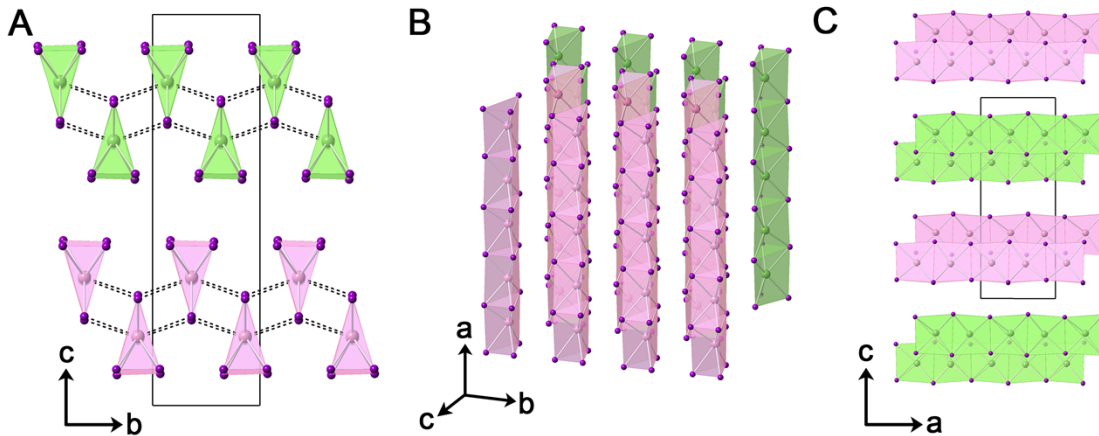


Figure 1: Crystal structure of  $\text{NbS}_3$ -IV. Panel A shows the view down the chains (down the *a*-axis). Alternating bilayers are colored green and pink, with the van der Waals gap located between them. Dashed lines indicate interchain interactions. The unit cell is outlined in black. Panel B shows an angled perspective view that highlights the stacked trigonal prismatic units that comprise each  $\text{NbS}_3$  chain. The view down the *b*-axis (panel C) reveals the parallel chains oriented along the *a*-axis.

Although the structural differences among NbS<sub>3</sub> polymorphs are relatively small, they contribute to diverse electronic properties. Transport measurements and/or calculations indicate that NbS<sub>3</sub>-I and -IV are semiconducting whereas NbS<sub>3</sub>-II and -V are metallic, with NbS<sub>3</sub>-II experimentally exhibiting several charge density wave transitions (9-11). As pointed out by Canadell and coworkers, “the extra electron provided by the transition metal atom in group V trichalcogenides may be used to induce either (i) metal-metal bonding (i.e. commensurate or incommensurate CDW or Peierls distortions) or (ii) S-S bond reduction (9).”

Like other transition metal trichalcogenides, NbS<sub>3</sub> can be nanostructured by exfoliation, i.e., mechanical and chemical methods that cleave the quasi-1D structure along the van der Waals gap, yielding nanoribbons and nanowires suitable for device fabrication. As an example, one recent report described a polarization photodetection device based on mechanically exfoliated NbS<sub>3</sub>-I (12).

Understanding a nanomaterial’s chemical and structural features is essential for successful device processing and high-performance applications. Important factors include (i) the details of nanoscale topography, especially at critical interfaces, (ii) the presence and concentration of defects (atomic substitutions, vacancies, disorder at grain boundaries, reactive dangling bonds), and (iii) the identity, distribution, and evolution of phases with respect to temperature, time, irradiation, and other conditions relevant to material processing and device performance.

The results described in this contribution illuminate some of these factors with respect to NbS<sub>3</sub>-IV nanoribbons. Specifically, we use *in situ* electron microscopy imaging and analysis to observe the dynamics of NbS<sub>3</sub>-IV nanoribbons at temperatures between room temperature (RT) and 1000 °C. *In situ* electron microscopy provides excellent tools with which to observe morphological and atomic changes. Such studies of MoS<sub>2</sub> nanomaterials under [ultra-high vacuum conditions](#) have helped establish detailed mechanisms for transformations that occur upon heating (13-15). To date, however, there has been a single study of metal *trichalcogenide* dynamics at the nanoscale: a 1987 report by Danot and coworkers describing electron diffraction of NbS<sub>3</sub>-I between RT and 500 °C (16). These authors concluded that NbS<sub>3</sub>-I converts to Nb<sub>1.2</sub>S<sub>2</sub>, a 3*R*-type polymorph of NbS<sub>2</sub> containing excess intercalated Nb, upon heating at 500 °C for 20 h.

Our study of NbS<sub>3</sub>-IV nanoribbons is based on a unique combination of two scanning transmission electron microscopes, each with distinctive capabilities that enable complementary imaging and analysis modalities—secondary electron (SE) imaging, bright field (BF) imaging, high angle annular dark field (HAADF) imaging, and electron energy loss spectroscopy (EELS)—while conducting *in situ* heating experiments (17-20). The first of these microscopes, a low kV Scanning Transmission Electron [Microscope](#) (STEM), allows us to monitor changes in internal and surface morphology as NbS<sub>3</sub>-IV nanoribbons change with increasing temperature. The second microscope, an aberration-corrected STEM with high resolution EELS, provides atomic and chemical information under similar conditions. By integrating the resulting data sets, we are able to construct a comprehensive picture of the chemical and structural changes occurring during the thermal breakdown of NbS<sub>3</sub>-IV nanoribbons, which we present here.

## Results and Discussion:

Solvent exfoliated NbS<sub>3</sub>-IV samples with nanoribbon morphology were used for the *in situ* experiments. These nanoribbons are long and narrow (aspect ratio  $\gg 10$ ). As illustrated in Figure S1, the highly-uniform image contrast in all three imaging modes indicates a highly homogenous sample with respect to composition and texture. Dispersions of NbS<sub>3</sub>-IV nanoribbons were transferred onto microelectromechanical system (MEMS) chips that interface with heating stages in each microscope for temperature regulation during data collection.

Advantageously, using low kV STEM allows for simultaneous imaging of both the sample exterior with the secondary electron (SE) detector and internal structural features with bright field (BF) and high angle dark field (HAADF) detectors. Figure 2 shows the major morphological changes visible by these imaging modes while heating NbS<sub>3</sub>-IV nanoribbons at a rate of five degrees per second. Figure 2 includes highlights at RT, 500 °C, and 1000 °C; the SI includes data recorded at 100-degree increments.

At RT (Figure 2A–C), we see a single, ~200-nm wide NbS<sub>3</sub>-IV nanoribbon; the BF and HAADF images indicate a smaller width of ~170 nm, which is consistent with the presence of an organic overlayer visible in SE mode (Figure 2A-C). The vertical striations in panels B and C are consistent with the quasi-1D structure of NbS<sub>3</sub>-IV, which leads to cleavage features along the material's chains (*a*-axis). Prior AFM studies have shown these parallel stripes correspond to bundles or plateaus of metal trichalcogenide chains (21).

As the sample is heated, the overlayer dissipates by 200 °C, revealing a relatively smooth surface (SI Figure S2). Once the sample reaches 500 °C, we begin to see new features on the wires surface in the SE imaging mode (Figure 2D) in conjunction with changes in contrast by BF and HAADF (Figures 2E–F). The mottled appearance of the nanoribbon (Figure 2F) corresponds to structural deformations caused by regions gaining or losing atomic density. In all three imaging modes, a certain amount of ribbing along the *a*-axis is visible.

As heating progresses past 500 °C, the darker/denser areas expand across the entire nanoribbon and develop into angular grains (SI Figure S2). By 1000 °C, the sample is fully reconstructed, although the overall nanoribbon morphology is preserved (Figure 2G–I). SE

imaging reveals that the material's surface has become highly textured with hexagonal and trapezoidal plateaus and divots. Interestingly, delamination along the nanoribbon has caused some edge sections to become detached (Figure 2G, arrow). BF and HAADF imaging also reveal polyhedral grains through and along the nanoribbon (Figure 2H-I). The overall width has been reduced to  $\sim 152$  nm, indicating that material consolidation has occurred.

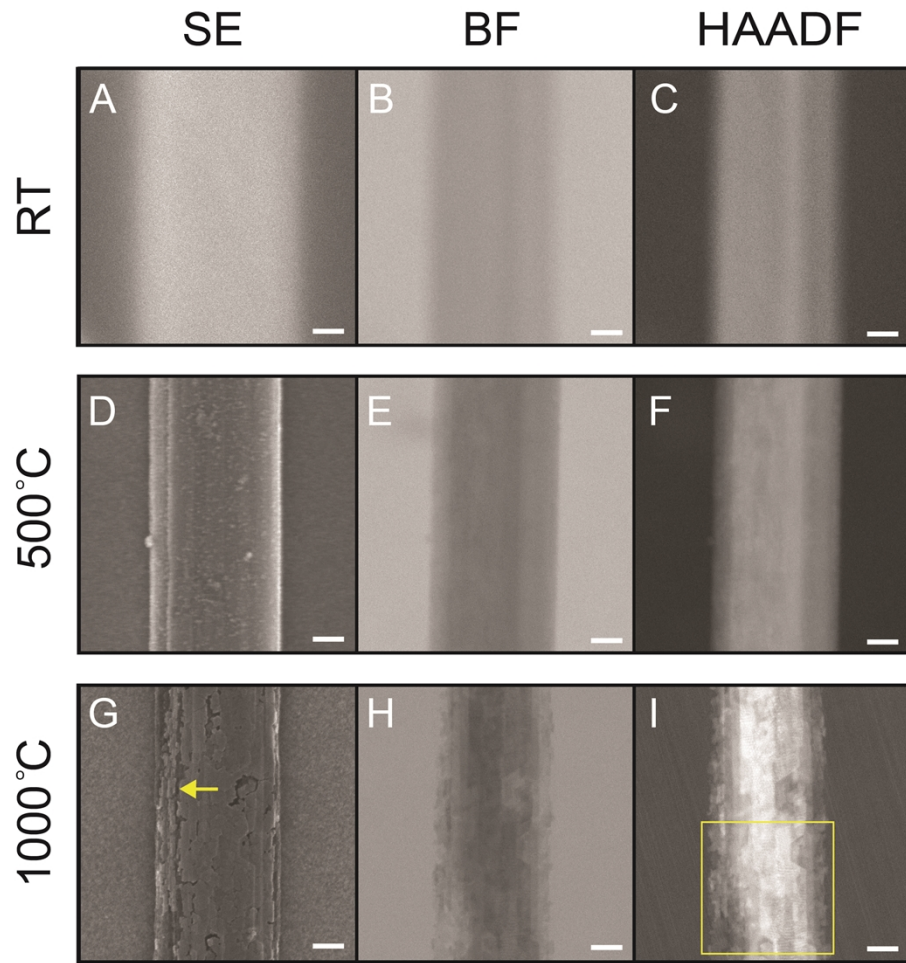


Figure 2: Low kV analysis of a NbS<sub>3</sub>-IV nanoribbon at increasing temperatures. This representative sample was imaged using secondary electron (SE), bright field (BF) and high angle annular dark field (HAADF) modes with the Hitachi SU9000EA microscope. The initial NbS<sub>3</sub>-IV nanoribbon at room temperature (panels A–C) exhibits structural changes by 500 °C (panels D–F), which are especially visible in BF and HAADF modes.

By 1000 °C, all images reveal extensive material reconstruction (panels G–I), although the overall nanoribbon morphology is retained. The yellow boxes in panels G–I and arrow in G correspond to details shown in Figure 3. Scale bars equal 50 nm.

The structural changes become clearer at higher magnification (Figure 3). The SE image shows layered, polyhedral features on top of larger flat areas. This topography includes numerous cracks and complex edge structures (Figure 3A). BF imaging reveals sub-10 nm particles along the nanoribbon’s perimeter, as well as larger trapezoidal features (Figure 3B). Furthermore, there appear to be long, vertical grains or “planks” in the structure that correlate to areas that the stepped polyhedral regions were growing on. HAADF imaging highlights the consolidation of material toward the nanoribbon’s core, as indicated by its brightness compared to the thinner periphery (Figure 3C). Also, as in the case of the SE image, the HAADF images exhibit what appears to be a horizontal alignment in the newly formed polyhedral steps.

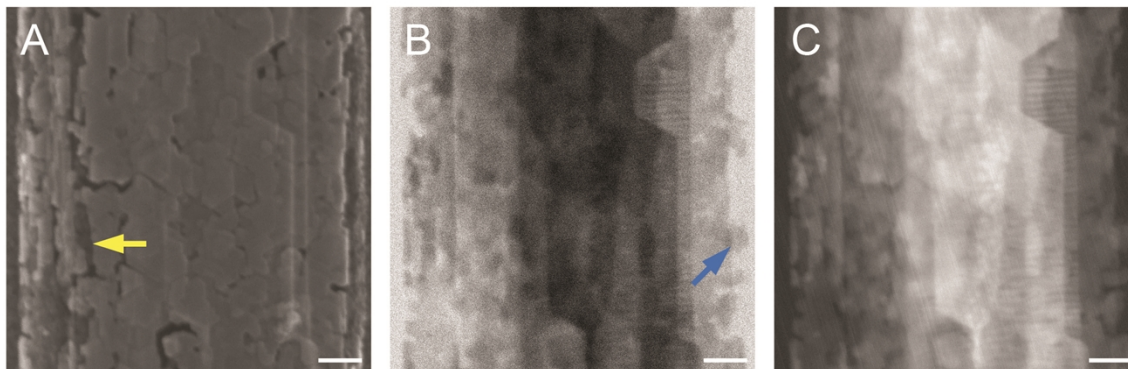


Figure 3: Higher magnification views of a niobium sulfide sample at 1000 °C (yellow-boxed area from Figure 2G–I). The yellow arrow in the SE image (A) indicates an area of delamination, and plentiful hexagonal grains are visible across the sample’s surface. BF (B) and HAADF (C) images reveal long vertical grains (planks) throughout the sample. The blue arrow points toward a sub-10 nm particle on the sample’s surface. Scale bars equal 20 nm.

To clarify the atomic basis of these changes, similar *in situ* heating experiments were conducted using the Nion UltraSTEM 100 microscope to collect atomic resolution HAADF images and EELS data. As shown in Figure 4A, a NbS<sub>3</sub>-IV nanoribbon at RT

presents well-resolved, parallel niobium sulfide chains with an experimental spacing of 0.526 nm, which compares favorably to a theoretical value of 0.497 nm, as well as a distinct orthogonal pattern due to niobium–niobium pairing along these chains; the atomic details of this feature can be seen clearly by HR-TEM (SI Figure S3). The FFT of the atomic resolution image was indexed to the [001] zone axis of NbS<sub>3</sub>-IV using  $d_{100}$  and  $d_{010}$  measurements of 0.679 and 0.492 nm, respectively, which are in close agreement with the calculated values of 0.675 and 0.497 nm from the crystal structure (Figure 4A inset).

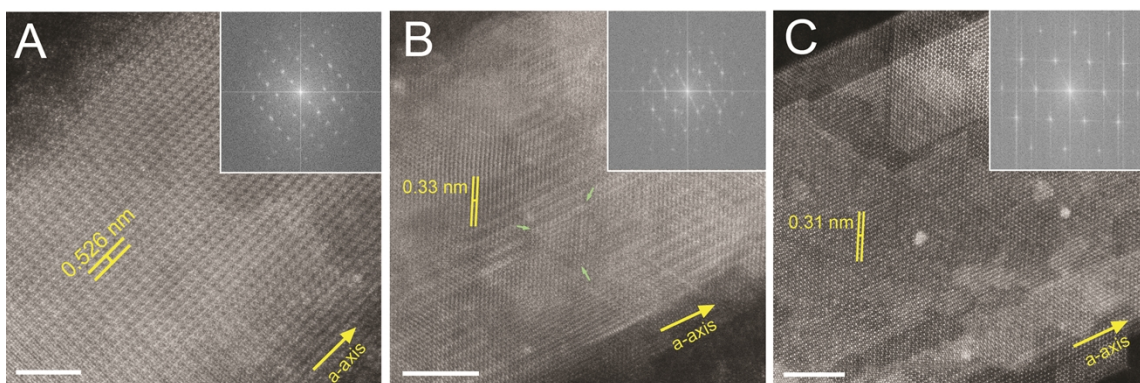


Figure 4: Atomic resolution STEM imaging (Nion UltraSTEM 100) of a niobium sulfide nanoribbon at increasing temperatures. (A) RT image and FFT (inset) are consistent with the starting material, NbS<sub>3</sub>-IV. (B) Image at 500 °C; the existence of triangular grains (green arrows at the vertex points) and a more complex FFT (inset) indicate the presence of mixed phases. (C) Data at 1000 °C are consistent with polyhedral grains of NbS<sub>2</sub>. All FFTs correspond to the entire ribbon region shown in the panel. Scale bars equal 5 nm.

Upon reaching 500 °C, many differences immediately become visible (Figure 4B). One striking change is the appearance of bright lines at 60° and 120° with respect to the original NbS<sub>3</sub> chains, with some of them outlining triangular grains (Figure 4B, green arrows). The formation of such triangular crystals is a distinctive feature of many transition metal dichalcogenide systems, including NbS<sub>2</sub> (22-24). Although NbS<sub>3</sub>-IV chains are present, new atomic rows in various orientations indicate that a structural transformation is underway. For example, the most prevalent spacing between the newly formed rows is 0.33 nm, smaller than that ~0.5 nm seen for NbS<sub>3</sub>. The FFT contains several identifiable patterns including the original RT pattern of NbS<sub>3</sub>-IV, a new diamond-shaped configuration, and a nascent ring (Figure 4B inset, Figure S4). Furthermore, the FFTs from

5 nm domains of this nanoribbon at 500 °C exhibit a variety of patterns and orientations consistent with polycrystallinity (Figure S5).

Imaging at 1000 °C reveals a completely altered atomic structure (Figure 4C) compared to the starting material (Figure 4A). The quasi-1D chains have been replaced by horizontally stepped layers with polyhedral islands and a hexagonal atomic structure. FFT analysis provides *d*-spacing values of 0.302, 0.301, and 0.175 nm, consistent with the (010), (100), and (110) lattice planes of NbS<sub>2</sub>, respectively, oriented along the [001] zone axis (Figure 4C). Although these values are most consistent with the 1*T* phase of NbS<sub>2</sub> (Table S1) (25), several factors mitigate this assignment: (i) trigonal prismatic coordination is strongly favored in the NbS<sub>2</sub> system, i.e., the 2*H* and 3*R* polymorphs are almost always isolated, and 2*H* is considered the thermodynamically-stable phase (26); there have been only a few reports of NbS<sub>2</sub> containing octahedral niobium (1*T*-NbS<sub>2</sub>) as monolayers or thin film samples (27, 28); (ii) it is often not straightforward to unambiguously distinguish these polymorphs by diffraction, especially in this sample orientation (29); and (iii) 3*R*-NbS<sub>2</sub> usually forms from the elements under stoichiometric or sulfur deficient conditions (29, 30). These factors lead us to believe that the niobium sulfide phase formed in our *in situ* experiments at 1000 °C is likely 2*H*-NbS<sub>2</sub>, pending future confirmation by *in situ* temperature-dependent Raman spectroscopy.

Figure 5 presents high-resolution dark field STEM images of the same nanoribbon at 1000 °C. In Figure 5A, imaging shows that the end of the nanoribbon is composed of regions of varying thickness, which can be distinguished by their relative contrast in HAADF mode. Each of these layers is outlined with a different color in panel 5B. The layers adopt irregular shapes composed of intergrown triangles and hexagons, and additional smaller islands (blue outline) and divots (purple outline) can be identified. All grain boundaries are atomically sharp. The well-resolved hexagonal lattice (Figure 5C) is characteristic of monolayer transition metal dichalcogenides as well as multilayer 2*H*-phases like 2*H*-MoS<sub>2</sub> and 2*H*-TaS<sub>2</sub> (31). The fine atomic structure is also visualized, most notably seen by the bright niobium atoms in the hexagonal atomic arrangement with bond distances of 0.21 nm between neighboring atoms and 0.46 nm across the hexagon (Figure 5C). Moreover, in this image, there is a step in thickness from one layer to another as evidenced by the contrast drop in the hexagonal shape of the atomic layers continuing

across the variation in height. In addition, the region encompassed by panel C appears free of vacancies or other defects.

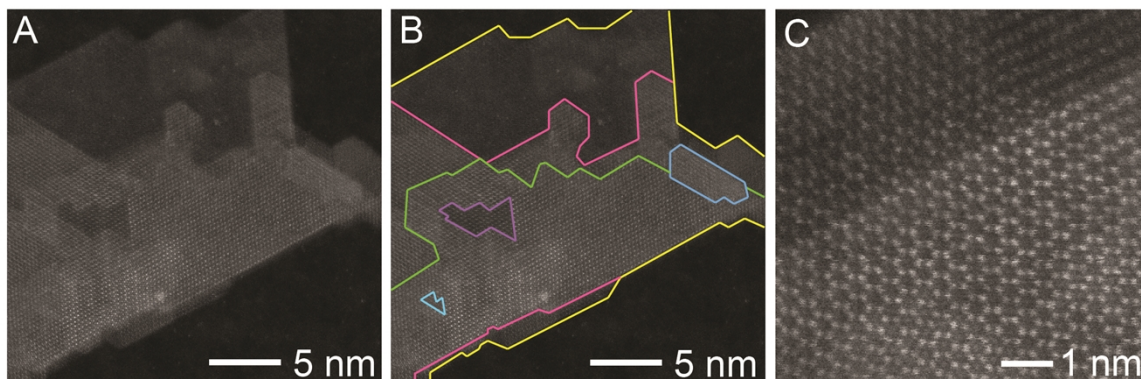


Figure 5: Atomic-scale dark field imaging (Nion UltraSTEM 100) of a niobium sulfide nanoribbon at 1000 °C. Panels A and B show that the nanoribbon is now composed of layered grains; six distinct regions with varying thicknesses are outlined in different colors. Panels C shows a higher magnification view of the hexagonal atomic structure.

During our work with  $\text{NbS}_3$  polymorphs, we have noted numerous instances of chain twisting visible by high resolution electron microscopy. One example is shown in Figure 6A: this  $\text{NbS}_3$ -IV nanoribbon at RT contains a twisted  $\text{NbS}_3$  chain (between parallel yellow lines within the yellow box). The  $60^\circ$  twist that is visible spans 6–7 nm, as indicated by the arrows. Perhaps importantly, this chain is located near the nanoribbon edge where it likely experiences less stabilization through interchain interactions with fewer neighboring chains than interior chains. Upon heating to 100 °C, this particular chain appears disordered (located between parallel green lines in Figure 6B) and may be in a transitional state from twisted to untwisted. Furthermore, FFT analysis shows a well-defined  $\text{NbS}_3$  pattern (straight chain) versus a smeared pattern (twisted chain) at RT, as well as a well-defined  $\text{NbS}_3$  pattern at 100 °C that corresponds to the now untwisted, straight chain (SI Figure S6) (32). This observation suggests that annealing, even at such a low temperature, can allow twisted chains to relax into a more stable, straight alignment. Further investigations are needed to identify the prevalence of chain twisting in  $\text{NbS}_3$

samples and the impact of this novel defect on electronic properties, including charge density wave behavior.

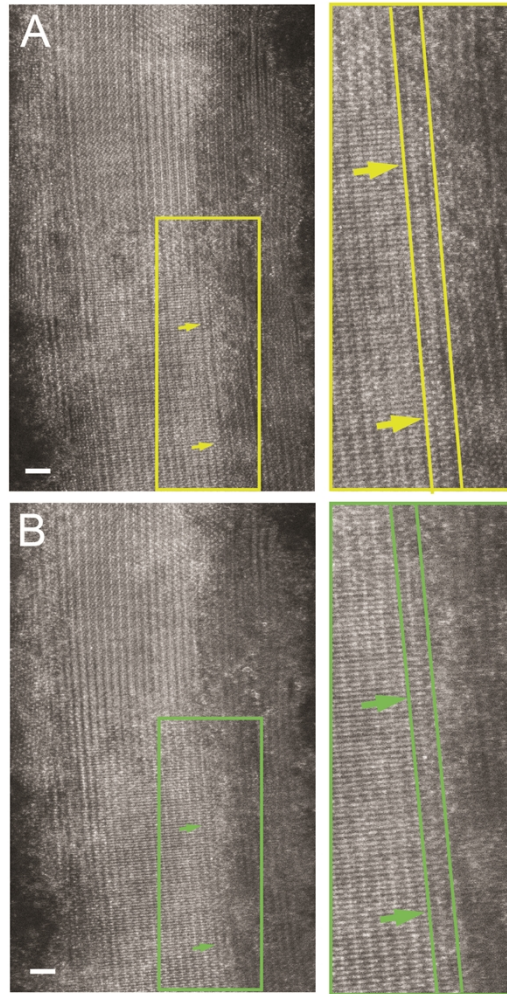


Figure 6: Atomic resolution STEM imaging (Nion UltraSTEM 100) of a  $\text{NbS}_3$ -IV nanoribbon that reveals the twisting and untwisting of an individual  $\text{NbS}_3$  chain. (A) As-prepared sample at RT. The yellow box highlights an area containing a single twisted  $\text{NbS}_3$  chain. In the magnified view at right, this chain is located between the parallel yellow lines; arrows indicate the length of this chain's  $60^\circ$  twist. (B) Sample heated to  $100^\circ\text{C}$  where only straight  $\text{NbS}_3$ -IV chains are visible in this image. All scale bars equal 1 nm.

Recent reports by Zettl and coworkers described metal trichalcogenide chains encapsulated within carbon or boron nitride nanotubes; in particular, single-, double-, and

triple-chain NbSe<sub>3</sub> adopts spiraling (helical torsional wave) morphologies with a wavelength for 2 $\pi$  rotation of 41 nm (33, 34). This value (6.8 nm for 60° rotation) is comparable to what we observe here for NbS<sub>3</sub>-IV. Although these encapsulation studies suggest that nanoconfinement is required to stabilize twisted metal trichalcogenide chains, here we see that twisted NbS<sub>3</sub> chains may be present within the crystalline lattice.

Electron energy loss spectroscopy (EELS) provides additional insight about the chemical transformations taking place during *in situ* heating. Figure 7 summarizes the HAADF intensities and EELS spectra taken across the main body of the nanoribbon sample at RT, 500 °C, and 1000 °C, SI Figure S7 displays the zones imaged on the nanoribbons from which the EELS spectra were collected. In Figure 7A, the HAADF intensity profiles reflect morphology changes related to the nanoribbon thinning across its width, i.e. consolidating towards the ribbons' core, as well as the stepped nature of the newly formed grains. The shaded region within Figure 7A corresponds to the area analyzed by EELS, the specific spectra of which are seen in panels 7B and 7C. By specifically investigating the higher energy signals (60–70 eV for Nb and 250–275 eV for S), we can see that the Nb intensity remains relatively constant between RT and 500 °C while the S intensity decreases significantly, with this trend continuing from 500 to 1000 °C (Figure 7B,C). This is strongly indicative of S loss from the nanoribbon as the chemical composition changes from NbS<sub>3</sub> to NbS<sub>2</sub>, which results in a higher relative amount of Nb per unit thickness. Moreover, the large difference seen in the S peak range is coming from a higher M4,5 cross-section, consistent with a change in the S bonding environment (Figure 7C). This chemical change is further highlighted in the EELS data from 500 °C and 1000 °C where there is a clear departure from the fine structure observed at lower temperature, further indicating bonding changes as noted by FFT (Figure 7C).

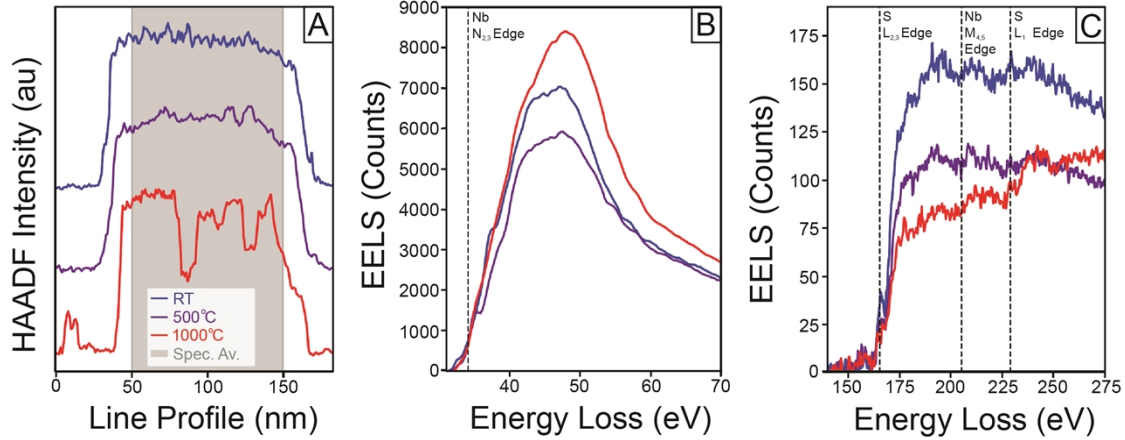


Figure 7: EELS analysis of a NbS<sub>3</sub>-IV nanoribbon at RT, 500 and 1000 °C. Panel (A) displays the HAADF intensity over the width of a representative nanoribbon, EELS spectra in panels B and C were collected from the region highlighted in gray. Panel (B) shows the Nb edges of the EELS spectra between 30-70 eV and (C) shows the fine structure of S and Nb signals after background subtraction in the region of 150-275 eV.

The excellent spatial resolution of EELS also allows us to probe signals originating from the thicker and thinner parts of the nanoribbon (SI Figure S8). When probing these localized areas, we see many of the same heat-induced changes, such as the significantly greater thickness of the nanoribbon at RT compared to the sample at 500 and 1000 °C, and the increase in the relative amount of Nb in the structure at 1000 °C. Importantly, the localized EELS data show that the depressed regions in the main body of the nanowire at 1000 °C have the same spectral characteristics as the raised regions, indicating that the variances observed in HAADF intensity are caused by changes in step and island heights rather than atomic structure or composition (SI Figure S8).

Based on these data, we present a mechanism for the changes that occur when NbS<sub>3</sub>-IV nanoribbons are heated. As shown in detail by Figure 8A, the structure of NbS<sub>3</sub>-IV is based on stacked trigonal prismatic niobium hexasulfide units, within which the bonding can be described as Nb<sup>4+</sup>(S<sub>2</sub>)<sup>2-</sup>-S<sup>2-</sup>. Every other pair of stacked niobium hexasulfide units contains Nb–Nb bonding, i.e., Nb1–Nb2 pairs at a distance of 3.045 Å. In addition, Nb–S interchain interactions define chain bilayers into 2D sheets. It seems most likely that the sulfur released upon heating corresponds to one atom from each (S<sub>2</sub>)<sup>2-</sup>, i.e.,

(S1,S2)<sup>2-</sup> or (S4,S5)<sup>2-</sup>, which are less strongly bound to niobium than the S<sup>2-</sup> coordinated between niobium centers across the van der Waals gap, i.e., S3 or S6. One sulfur from each of these (S<sub>2</sub>)<sup>2-</sup> is labeled in yellow (Figure 8A). Upon loss of this sulfur by 500 °C, relatively small atomic movements are needed to facilitate bond formation between each niobium and two additional sulfur atoms from adjacent chains, which is aided by the pre-existing Nb---S interactions. This results in half of a new niobium hexasulfide polyhedron, the building block of NbS<sub>2</sub>. Furthermore, sulfur loss from the NbS<sub>3</sub> structure causes the resulting NbS<sub>2</sub> nanoribbon to have greater atomic density and a reduced diameter across its width. As these chemical changes proceed, the niobium sulfides fuse to form continuous NbS<sub>2</sub> sheets of edge-sharing niobium hexasulfide polyhedra (Figure 8). These structural changes are reflected in the complex FFT at 500 °C (Figure 4B). In addition, the observed cracking (Figure 3) is consistent with the significant increase in material density, from 4.126 g cm<sup>-3</sup> for NbS<sub>3</sub>-IV to 4.4 g cm<sup>-3</sup> for NbS<sub>2</sub> (7, 25). The formation of NbS<sub>2</sub> is complete by 1000 °C and accompanied by nanoscale reconstruction into complex layered grains (Figures 3–5). Although the niobium hexasulfide polyhedra could adopt trigonal prismatic geometry (consistent with the 2*H* and 3*R* polymorphs of NbS<sub>2</sub>) or octahedral geometry (consistent with the 1*T* polymorph of NbS<sub>2</sub>), our preliminary conclusion is this product is most likely 2*H*-NbS<sub>2</sub>.

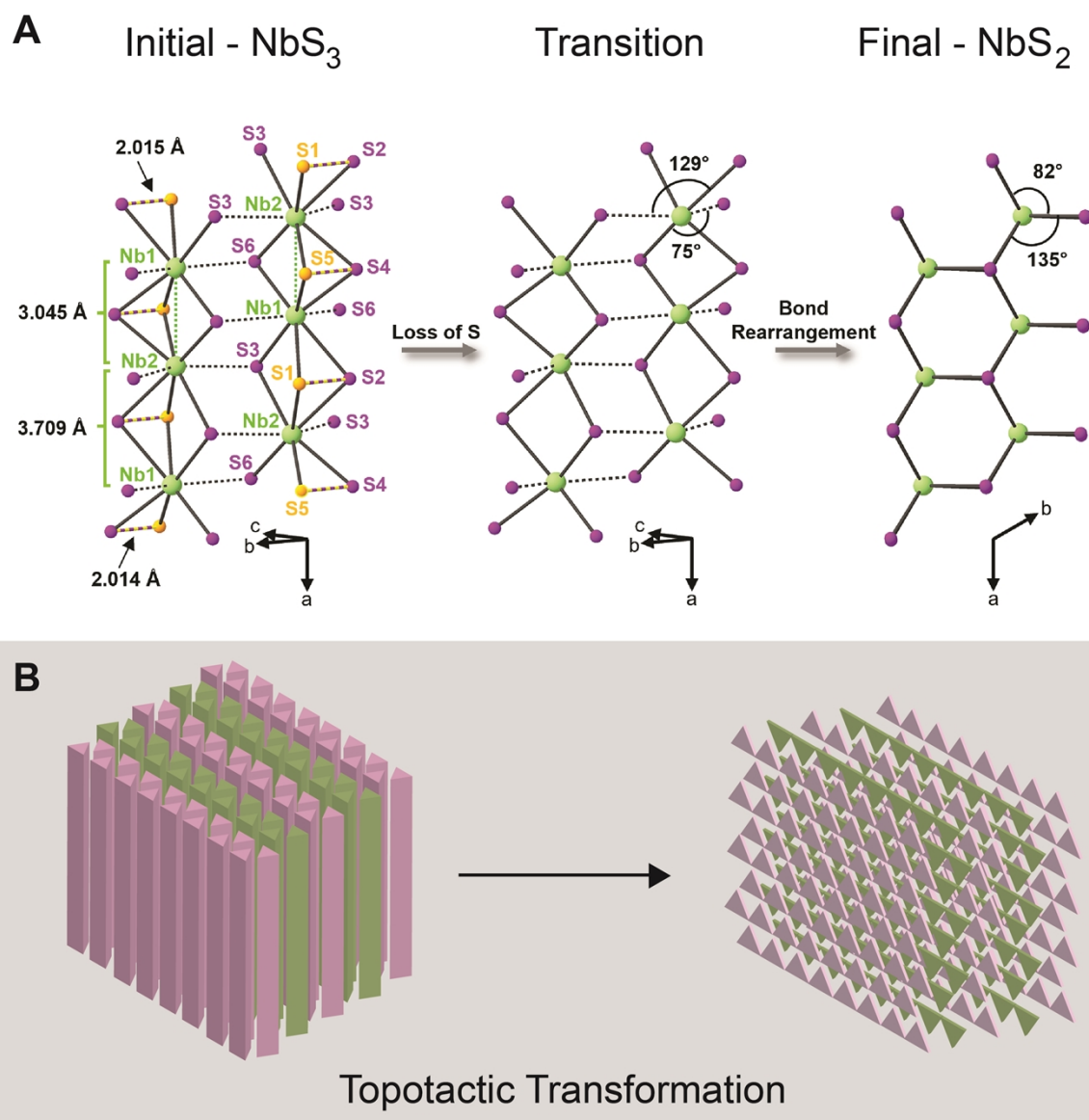


Figure 8: Panel A: Proposed mechanism of structural and compositional changes in NbS<sub>3</sub>-IV nanoribbons upon heating from RT to 1000 °C. This sequence of structures shows the loss of sulfur and additional atomic movements required to transform NbS<sub>3</sub>-IV into NbS<sub>2</sub>. Panel B: Schematic of overall structural and compositional changes in NbS<sub>3</sub>-IV nanoribbons upon heating from RT to 1000 °C, which highlights the topotactic nature of the NbS<sub>3</sub>-IV → NbS<sub>2</sub> transformation.

Because the overall NbS<sub>3</sub>-IV → NbS<sub>2</sub> reaction involves a NbS<sub>3</sub>-IV chain bilayer transforming into a NbS<sub>2</sub> monolayer, an important feature of this mechanism is its topotactic nature, which preserves the location of the van der Waals gap within the two lattices (Figure 8B). The final NbS<sub>2</sub> product maintains the overall morphology of the

starting NbS<sub>3</sub> nanoribbon, with minor alterations due to material migration and nanostructuring effects. The sequence illustrated in Figure 8A contrasts with a proposed mechanism of ZrS<sub>x</sub>Se<sub>2-x</sub> oxidation, which invokes collapse of the van der Waals gap through the formation of interlayer Zr–S and Zr–O bonds (35).

The NbS<sub>3</sub>-I → Nb<sub>1.2</sub>S<sub>2</sub> transformation mechanism proposed by Danot and coworkers entails a similar rearrangement as the one in Figure 8, which is not surprising due to the structural similarities between NbS<sub>3</sub>-I and NbS<sub>3</sub>-IV. However, they conclude that Nb<sub>1.2</sub>S<sub>2</sub> rather than stoichiometric NbS<sub>2</sub> forms under their experimental conditions. Certainly Nb<sub>1.2</sub>S<sub>2</sub> is a known phase, but no definitive evidence for Nb<sub>1.2</sub>S<sub>2</sub> vs. NbS<sub>2</sub> was provided by Danot and coworkers. Furthermore, according to *ex situ* studies, heating NbS<sub>3</sub>-I at 800 °C for 1.5 h leads to 2H-NbS<sub>2</sub> (36). We also do not find evidence of Nb<sub>1.2</sub>S<sub>2</sub>, although our samples are not in the optimal orientation to detect Nb intercalation. Mechanisms similar to that summarized in Figure 8 have been used by several research groups to explain the introduction of sulfur vacancies in TiS<sub>3</sub> and ZrS<sub>3</sub> (37, 38).

## Conclusions

In summary, a combination of *in situ* imaging and spectroscopy analysis tools have allowed us to construct a comprehensive picture of the structural changes experienced by NbS<sub>3</sub>-IV nanoribbons during thermal treatment. Low kV imaging with *in situ* heating revealed that the nanoribbon's originally smooth surface changes to one with a highly textured morphology comprised of polyhedral divots and plateaus throughout the structure. UltraSTEM imaging with *in situ* heating illuminated the transformation of aligned NbS<sub>3</sub>-IV chains into NbS<sub>2</sub> with complex layered morphologies. We also observed how moderate heating prompts the relaxation of NbS<sub>3</sub>-IV defects, specifically chain twisting, to improve interchain alignment. The correlated FFT and EELS data provided important information about the chemical changes taking place during the NbS<sub>3</sub>-IV → NbS<sub>2</sub> transformation, leading to a likely mechanism. Although chalcogen loss upon heating is generally well established for transition metal chalcogenides, the structural specifics of the NbS<sub>3</sub> system and the *in situ* experiments reported here allow us to propose a detailed atomistic mechanism for sulfur loss and subsequent rearrangements.

We anticipate that further insights will emerge from correlating the results of this study with macroscopic techniques, such as temperature-dependent and angle-resolved Raman spectroscopy (under UHV and/or inert atmosphere conditions) and neutron scattering. These techniques can provide potentially more detailed information about the alignment of NbS<sub>3</sub> chains and NbS<sub>2</sub> polytypes.

The results of this study will aid the preparation and processing of nanostructured NbS<sub>3</sub> for device incorporation (39-41). Intriguingly, these dynamics reflect the conversion of a quasi-1D quantum material, NbS<sub>3</sub>, into a 2D quantum material, NbS<sub>2</sub>, which is an area of significant interest as the development of low dimensional materials for quantum technologies accelerates. The integration of low kV imaging, UltraSTEM imaging, and EELS analysis provides an ideal platform for such studies.

## Experimental Details

### *Preparation of NbS<sub>3</sub>-IV Crystals:*

Niobium powder (99.99%) was purchased from Sigma-Aldrich, sulfur powder (>99.9%) from J.T. Baker, and bromine (>99%) from ACROS Organics. A stoichiometric mixture of 1.4753 g (15.9 mmol) niobium and 1.5647 g (48.8 mmol) sulfur was ground gently using an agate mortar and pestle. Next, 10.0  $\mu\text{L}$  of liquid bromine ( $2.1 \text{ mg cm}^{-3}$  for a  $\sim 15 \text{ cm}^3$  volume ampule) was micropipetted into a quartz glass ampule (10 mm ID, 14 mm OD, 170 mm length) suspended in an acetonitrile/dry ice bath, followed by the addition of the ground powder mixture. The ampule was evacuated and backfilled with Ar three times before being vacuum sealed ( $10^{-2}$  Torr) and placed in a three-zone furnace. The reaction was heated at a rate of  $5 \text{ }^\circ\text{C min}^{-1}$  to 670–570  $^\circ\text{C}$  (source zone–growth zone) for 10 d. After heating was complete, the ampule was left in the furnace to cool naturally to room temperature. The resulting dark gray fibers of NbS<sub>3</sub>-IV were collected and placed in a vacuum oven at room temperature for 30 mins to remove residual bromine.

*Exfoliation of NbS<sub>3</sub>-IV Crystals into Nanoribbons:* 4.7 mg of NbS<sub>3</sub>-IV crystals were added to  $\sim 12 \text{ mL}$  of acetone in a 50 mL centrifuge tube. This sample was probe sonicated at 28 Amp for 1 h. After sonication, the sample was allowed to sit until larger particles settled (15–30 min). The decanted supernatant containing NbS<sub>3</sub>-IV nanoribbons was used for electron microscopy.

### *Microscopy:*

In situ imaging of NbS<sub>3</sub>-IV with the Hitachi SU9000EA low KV STEM instrument was conducted using an accelerating voltage of 30 kV and a current of 10  $\mu\text{A}$ . Exfoliated NbS<sub>3</sub>-IV dispersed in acetone was brushed onto the heating portion of a four contact Norcada micro-electromechanical heating chip, with 2–3  $\mu\text{m}$  diameter holes. The chip was then placed onto a single tilt Hitachi Blaze heating holder that was then inserted into the microscope. Initial images were taken and the sample was then heated at a rate of  $5 \text{ }^\circ\text{C s}^{-1}$  to the respective imaging temperature in 100 degree increments. All images were collected

simultaneously with the secondary electron, bright field, and high angle dark field detectors.

In situ imaging and analysis with the Nion UltraSTEM 100. As synthesized NbS<sub>3</sub> (iv) nanowires were dispersed in isopropanol and brushed onto the heating portion of a Protochips mems chip and heated at a rate of 5 °C s<sup>-1</sup> to the respective imaging and analysis temperature.

For STEM imaging and EELS, data were acquired in 100 °C increments from RT to 1000 °C. Because the heating process induces significant drift, the sample stage must be allowed to thermally equilibrate prior to data collection. This requirement precludes direct observations during temperature ramping.

A Thermo Fisher Titan STEM was also used for non in situ imaging of the NbS<sub>3</sub> nanoribbons.

#### *Data Processing:*

Images were processed to maximize brightness and contrast in Photoshop. All measurements were conducted in ImageJ.

#### **References**

1. Island, J. O.; Molina-Mendoza, A. J.; Barawi, M.; Biele, R.; Flores, E.; Clamagirand, J. M.; Ares, J. R.; Sánchez, C.; Van Der Zant, H. S. J.; D'Agosta, R. "Electronics and Optoelectronics of Quasi-1D Layered Transition Metal Trichalcogenides," *2D Materials*, **2017**, *4*, 022003.
2. Geremew, A.K.; Rumyantsev, S.; Bloodgood, M.A.; Salguero, T.T.; Balandin, A.A. "Unique features of the generation-recombination noise in quasi-one-dimensional van der Waals nanoribbons," *Nanoscale*, **2018**, *10*, 19749-19756.
3. Geremew, A.; Bloodgood, M.A.; Aytan, E.; Woo, B.W.K.; Corber, W.R.; Liu, G.; Bozhilov, K.; Salguero, T.T.; Rumyantsev, S.; Rao, M.P.; Balandin, A.A. "Current Carrying Capacity of Quasi-1D ZrTe<sub>3</sub> Van der Waals Nanoribbons," *IEEE Electron Device Letters*, **2018**, *39*, 735-738.
4. Patra, A.; Rout, C.S. "Anisotropic quasi-one-dimensional layered transition-metal trichalcogenides: synthesis, properties and applications," *RSC Adv.*, **2020**, *10*, 36413.

5. Wen, X.; Lei, W.; Ni, L.; Yang, L.; Zhang, P.; Liu, Y.; Chang, H.; Zhang, W. "Evaluating the Electrical Characteristics of Quasi-One-Dimensional ZrTe<sub>3</sub> Nanoribbon Interconnects," *ACS Appl. Electron. Mater.*, **2021**, *3*, 4228-4235.
6. Rijnsdorp, J.; Jellinek, F. "The Crystal Structure of Niobium Trisulfide, NbS<sub>3</sub>," *J. Solid State Chem.*, **1978**, *25*, 325–328.
7. Bloodgood, M. A.; Wei, P.; Aytan, E.; Bozhilov, K. N.; Balandin, A. A.; Salguero, T. T. "Monoclinic Structures of Niobium Trisulfide," *APL Mater.*, **2018**, *6*, 026602.
8. Zupanič, E.; van Midden, H. J. P.; van Midden, M. A.; Šturm, S.; Tchernychova, E.; Pokrovskii, V. Y.; Zytsev, S. G.; Nasretdinova, V. F.; Zaitsev-Zotov, S. V.; Chen, W. T.; Pai, W. W.; Bennett, J. C.; Prodan, A. "Basic and charge density wave modulated structures of NbS<sub>3</sub>-II," *Phys. Rev. B*, **2018**, *98*, 174113.
9. Conejeros, S.; Guster, B.; Alemany, P.; Pouget, J.P.; Canadell, E. "Rich Polymorphism of Layered NbS<sub>3</sub>," *Chem. of Mater.*, **2021**, *33*, 5449-5463.
10. Monceau, P. "Electronic Crystals: An Experimental Overview," *Advances in Physics*, **2012**, *61*, 325-581.
11. Zytsev, S.G.; Pokrovskii, V. Y.; Nasretdinova, V. F.; Zaitsev-Zotov, S. V.; Pavlovskiy, V.V.; Odobesco, A. B.; Pai, W. W.; Chu, M. W.; Lin, Y. G.; Zupanic. E.; van Midden, H. J. P.; Sturm, S.; Tchernychova, E.; Prodan, A.; Bennett, J.C.; Mukhamedshin, I. R.; Chernysheva, O. V.; Menushenkov, A. P.; Loginov, V. B.; Loginov, B. A.; Titov. A. N.; Abdel-Hafiez, M. "Basic and charge density wave modulated structures of NbS<sub>3</sub>-II," *Phys. Rev. B*, **2017**, *95*, 035110.
12. Wang, Y.; Wu, P.; Wang, Z.; Luo, M.; Zhong, F.; Ge, X.; Zhang, K.; Peng, M.; Ye, Y.; Li, Q.; Ge, H.; Ye, J.; He, T.; Chen, Y.; Xu, T.; Yu, C.; Wang, Y.; Hu, Z.; Zhou, X.; Shan, C.; Long, M.; Wang, P.; Zhou, P.; Hu, W. "Air-stable Low Symmetry Narrow Bandgap 2D Sulfide Niobium for Polarization Photodetection" *Adv. Mater.*, **2020**, *32*, 2005037.
13. Sang, X.; Li, X.; Puretzky, A. A.; Geohegan, D. B.; Xiao, K.; Unocic, R. R. "Atomic Insight into Thermolysis-Driven Growth of 2D MoS<sub>2</sub>," *Adv. Func. Mater.*, **2019**, *29*, 1902149.
14. Fei, L.; Lei, S.; Zhang, W. B.; Lu, W.; Lin, Z.; Lam, C. H.; Chai, Y.; Wang, Y. "Direct TEM observations of growth mechanisms of two-dimensional MoS<sub>2</sub> Flakes," *Nature Comm.*, **2016**, *7*, 12206.
15. Zink, N.; Therese, H. A.; Pansiot, J.; Yella, A.; Banhart, F.; Tremel W. "In Situ Heating TEM Study of Onion-like WS<sub>2</sub> and MoS<sub>2</sub> Nanostructures Obtained via MOCVD," *Chem. Mater.*, **2008**, *20*, 65-71.

16. Kurdi, M.; Marie, A.-M.; Danot, M. "The Crystallographic Mechanism of the NbS<sub>3</sub> to Nb<sub>1.2</sub>S<sub>2</sub> Transition," *Solid State Comm.*, **1987**, *64*, 395-399.
17. Schurmann, U.; Winkler, M. Konig, J. D.; Liu, X.; Duppel, V.; Bensch, W.; Bottner, H.; Kienle, L. "In Situ TEM investigations on Thermoelectric Bi<sub>2</sub>Te<sub>4</sub>/Sb<sub>2</sub>Te<sub>3</sub> Multilayers," *Adv. Eng. Mater.*, **2012**, *14*, 139-143.
18. Liu, C.; Malladi, S. K.; Xu, Q.; Chen, J.; Tichelaar, F. D., Zhuge, X.; Zandbergen, H. W. "In situ STEM imaging of growth and phase change of individual CuAl<sub>x</sub> precipitates in Al alloy," *Scientific Reports*, **2017**, *7*, 2184.
19. Liu, X.; Wood, J. D.; Chen, K. S.; Cho, E.; Hersam, M. C. "In Situ Thermal Decomposition of Exfoliated Two-Dimensional Black Phosphorous," *J. Phys Chem. Letter*, **2015**, *6*, 773-778.
20. Xu, F.F.; Ebina, Y.; Bando, Y.; Sasaki, T. "In Situ Transmission Electron Microscopic Study of Perovskite-Type Niobate Nanosheets under Electron-Irradiation and Heating," *J. Phys. Chem. B*, **2003**, *107*, 66698-666703.
21. Lipatov, A.; Loes, M.J.; Lu, H.; Dai, J.; Patoka, P.; Vorobeva, N.S.; Muratov, D.S.; Ulrich, G.; Kästner, B.; Hoehl, A.; Ulm, G.; Zeng, X.C.; Rühl, E.; Gruverman, A.; Dowben, P.A.; Sinitskii, A. "Quasi-1D TiS<sub>3</sub> Nanoribbons: Mechanical Exfoliation and Thickness-Dependent Raman Spectroscopy," *ACS Nano*, **2018**, *12*, 12713-12720.
22. Tang, L.; Tan, J.; Nong, H.; Liu, B.; Cheng, H.M. "Chemical Vapor Deposition Growth of Two-Dimensional Compound Materials: Controllability, Material Quality, and Growth Mechanism," *Acc. of Mater. Research*, **2021**, *2*, 36-47.
23. Ge, W.; Kawahara, K.; Tsuji, M.; Ago, H. "Large-scale synthesis of NbS<sub>2</sub> nanosheets with controlled orientation on graphene by ambient pressure CVD," *Nanoscale*, **2013**, *5*, 5773-5778.
24. Zhao, S.; Hotta, T.; Koretsune, T.; Watanabe, K.; Taniguchi, T.; Sugawara, K.; Takahashi, T.; Shinohara, H.; Kitaura, R. "Two-dimensional metallic NbS<sub>2</sub>: growth, optical identification and transport properties," *2D Materials*, **2016**, *3*, 025027.
25. Jellinek, F.; Brauer, G.; Mueller, H. "Molybdenum and Niobium Sulfides," *Nature*, **1960**, *185*, 376-377.
26. Ravnik, J.; Vaskivskiy, I.; Gerasimenko, Y.; Diego, M.; Vodeb, J.; Kabanov, V.; Mihailovic, D. "Strain Induced Metastable Topological Networks in Laser Fabricated TaS<sub>2</sub> Polytype, Heterostructures for Nanoscale Devices," *ACS Appl. Nano Mater.*, **2019**, *2*, 3743-3751.

27. Carmalt, C.J.; Manning, T.D.; Parkin, I.P.; Peters, E.S.; Hector, A.L. "Formation of a new (1T) trigonal NbS<sub>2</sub> polytype via atmospheric pressure chemical vapor deposition," *J. of Mater. Chem.*, **2004**, *14*, 290-291.
28. Leroux, M.; Cario, L.; Bosak, A.; Rodiere, P.; "Traces of charge density waves in NbS<sub>2</sub>," *Phys. Rev. B*, **2018**, *97*, 195140.
29. Witteveen, C.; Gornicka, K.; Chang, J.; Mansson, M.; Klimeczuk, T.; von Rohr, F.O. "Polytypism and superconductivity in the NbS<sub>2</sub> system," *Dalton Trans.*, **2021**, *50*, 3216-3223.
30. W. G. Fisher and M. Sienko, "Stoichiometry, structure, and physical properties of niobium disulfide," *Inorg. Chem.*, **1980**, *19*, 39-43.
31. Eda, G.; Fujita, T.; Yamaguchi, H.; Voiry, D.; Chen, M.; Chhowalla, M. "Coherent Atomic and Electronic Heterostructures of Single-Layer MoS<sub>2</sub>," *ACS Nano*, **2012**, *6*, 7311-7317.
32. Gailhanou, M.; Roussel, J.M. *J. Appl. Cryst.*, **2018**, *51*, 1-11.
33. Pham, T.; Oh, S.; Stetz, P.; Onishi, S.; Kisielowski, C.; Cohen, M.L.; Zettl, A. "Torsional instability in the single-chain limit of a transition metal trichalcogenide," *Science*, **2018**, *361*, 263-266.
34. Stonemeyer, S.; Cain, J.D.; Oh, Sehoon, Azizi, A.; Elasha, M.; Thiel, M.; Song, C.; Ercius, P.; Cohen, M.L.; Zettl, A. "Stabilization of NbTe<sub>3</sub>, VTe<sub>3</sub>, and TiTe<sub>3</sub> via Nanotube Encapsulation," *J. Am. Chem. Soc.*, **2021**, *143*, 4363-4568.
35. Jo, S.S.; Singh, A.; Yang, L.; Tiwari, S. C.; Hong, S.; Krishnamoorthy, A.; Sales, M.G.; Oliver, S. M.; Fox, J.; Cavalero, R. L.; Snyder, D. W.; Vora, P.M. McDonnell S.L.; Vashishta, P.; Kalliam R.K.; Nakano, A.; Jaramillo, R. "Growth Kinetics and Atomistic Mechanisms of Native Oxidation of ZrS<sub>x</sub>Se<sub>2-x</sub> and MoS<sub>2</sub> Crystal," *Nano Letters*, **2020**, *20*, 8592-8599.
36. Tao, Y.; Gao, Q.; Wang, X.; Wu, X.; Mao, C.; Zhu, J. "NbN and NbS<sub>2</sub> Nanobelt Arrays: In-Situ Conversion Preparation and Field-Emission Performance," *J. of Nanoscience and Nanotechnology*, **2011**, *11*, 3345-3349.
37. Tian, Z.; Han, C.; Zhao, Y.; Dai, W.; Lian, X.; Wang, Y.; Zheng, Y.; Shi, Y.; Pan, X.; Huang, Z.; Li, H.; Chen, W. "Efficient photocatalytic hydrogen peroxide generation coupled with selective benzylamine oxidation over defective ZrS<sub>3</sub> nanobelts," *Nature Comm.*, **2021**, *12*, 2039.

38. Tian, Z.; Guo, X.; Wang, D.; Sun, D.; Zhang, S.; Bu, K.; Zhao, W.; Huang, F. “Enhanced Charge Carrier Lifetime of TiS<sub>3</sub> Photoanode by Introduction of S<sub>2</sub><sup>2-</sup> Vacancies for Efficient Photoelectrochemical Hydrogen Evolution,” *Adv. Func. Mater.*, **2020**, *30*, 2001286.
39. Wu, W.; Wang, Y.; Niu, Y.; Wang, P.; Chen, M.; Sun, J.; Wang, N.; Wu, D.; Zhao, Z. “Thermal Localization Enhanced Fast Photothermoelectric Response in a Quasi-One-Dimensional Flexible NbS<sub>3</sub> Photodetector,” *ACS Appl. Mater. Interfaces*, **2020**, *12*, 14165-14173.
40. Wen, X.; Lei, W.; Ni, L.; Yang, L.; Zhang, P.; Liu, Y.; Chang, H.; Zhang, W. “Evaluating the Electrical Characteristics of Quasi-One-Dimensional ZrTe<sub>3</sub> Nanoribbon Interconnects,” *ACS Appl. Electron. Mater.*, **2021**, *3*, 4228-4235.
41. Wang, Y.; Wu, P.; Wang, Z.; Luo, M.; Zhong, F.; Ge, X.; Zhang, K.; Peng, M.; Ye, Y.; Li, Q.; Ge, H.; Ye, J.; He, T.; Chen, Y.; Xu, T.; Yu, C.; Wang, Y.; Hu, Z.; Zhou, X.; Shan, C.; Long, M.; Wang, P.; Zhou, P.; Hu, W. “Air-stable Low Symmetry Narrow Bandgap 2D Sulfide Niobium for Polarization Photodetection,” *Adv. Mater.*, **2020**, *32*, 2005037.

### **Acknowledgements:**

A portion of this research was conducted at the Center for Nanophase Materials Sciences, which is a DOE Office of Science User Facility. The Hitachi SU9000EA microscope used in this work was acquired with a Major Research Instrumentation (MRI) award from the U.S. National Science Foundation (award number 1919942).

### **Supporting Information:**

Additional images and spectroscopy data can be found in the supporting information.